Science Advances
AAAS

advances.sciencemag.org/cgi/content/full/6/21/eaaz8400/DC1

Supplementary Materials for

Chemiluminescence resonance energy transfer–based nanoparticles for quantum yield–enhanced cancer phototheranostics

Jueun Jeon, Dong Gil You, Wooram Um, Jeongjin Lee, Chan Ho Kim, Sol Shin, Seunglee Kwon, Jae Hyung Park*

*Corresponding author. Email: jhpark1@skku.edu

Published 20 May 2020, *Sci. Adv.* **6**, eaaz8400 (2020)
DOI: 10.1126/sciadv.aaz8400

This PDF file includes:

Supplementary Methods

Stability

In order to evaluate the kinetic stability of CRET-NPs, they were dispersed at a concentration of 0.5mg/ml in PBS (pH 7.4, 100 μM H_2O_2), standard simulated body fluid, or FBS-containing PBS (pH 7.4). The resulting solution was gently shaken at a speed of 100 rpm in the water bath at 37 ^oC. Thereafter, the changes in hydrodynamic sizes of the CRET-NPs were monitored as a function of times using Zetasizer (Nano ZS, Malvern Instruments Ltd., Worcestershire, UK).

In vivo biodistribution of CRET-NPs

All experiments with live animals were in compliance with relevant laws and institutional guidelines of Sungkyunkwan University, and institutional committees approved all experiments. To monitor the *in vivo* biodistribution of Ce6-NPs and CRET-NPs, HT29 tumor-bearing mice were prepared by injecting a suspension of 1×10^7 HT29 cells into subcutaneous tissue of nude mice (Orientbio Inc., Seongnam, Korea). When tumor volume of the HT29 tumor-bearing mice reached 150 - 200 mm^3, 200 μl of Ce6-NPs and CRET-NPs were intravenously injected into HT29 tumor-bearing BALB/c nude mice and monitored as a function of time. The *in vivo* fluorescence images were obtained using an IVIS Spectrum In Vivo Imaging System (PerkinElmer, Inc. MA, USA). Mice were sacrificed 24 h after intravenous injection of CRET-NPs. The dissected major organs and tumors were visualized using the IVIS Imaging System. All fluorescence images were obtained using wavelengths of 640 nm (excitation) and 720 (emission).

ESR spectroscopy

CRET-NPs and Ce6-NPs were dispersed at concentrations of 10 mg/ml in PBS (pH 7.4, 100 μM H_2O_2). 2 μl of TMP or DMPO was added into each solution and exposed to a 635 nm laser (50 mW/cm^2) for 10 min. Then, $^1O_2$ and free radicals were detected by ESR (Bruker Biospin EMXmicro, MA, USA).

Supplementary Results

Effects of TCPO content on CL imaging and ROS generation of CRET-NPs

To optimize the ratio of CL donor to CL acceptor, we prepared CRET-NPs using an o/w emulsion method by varying the weight ratio of TCPO and Ce6 set at 20:1, 10:1, 5:1, 3:1, 1:1, and 0:1. CRET-NPs, prepared at 20:1, were not used in the experiments because they were aggregated in the aqueous condition (Data not shown). CRET-NPs, prepared at 10:1, showed the strongest CL signal in the presence of H_2O_2, and the signals were gradually decreased as the TCPO content decreased in the NPs (fig. S4A). As expected, the CL signal was dependent on the concentration (fig. S4B). The CL images of CRET-NPs at various weight ratios were also obtained using an optical imaging system after their subcutaneous injections (with 100 μM H_2O_2) into BALB/c nude mice (fig. S5). A strongest CL signal of CRET-NPs, prepared at 10:1, was detected in the lower back of the mice (fig. S5A). Quantitatively, a CL signal intensity of CRET-NPs, prepared at 10:1, was at least 3.4 times higher than those of other CRET-NPs (fig. S5B).

We next measured ROS generation behaviors under laser irradiation by free Ce6 and various types of CRET-NPs using the RNO assay (fig. S6). The amount of ROS generated by CRET-NPs, prepared at 10:1, was higher than those of other CRET-NPs. In general, the ROS generation rate of Ce6-loaded NPs was slower than that of free Ce6, due to the

self-quenching properties of the NPs. Interestingly, the ROS generation rate of CRET-NPs, prepared at 10:1, was comparable to that of free Ce6. Therefore, CRET-NPs, prepared at 10:1, were used for all subsequent experiments.

In vivo distribution of CRET-NPs

After optimize the ratio of CL donor to CL acceptor, we then investigated the *in vivo* biodistribution of CRET-NPs after intravenous injection into mice with HT29 tumor-bearing BALB/c nude mice and monitored as a function of time (fig. S7). A strong fluorescence intensity of CERT-NPs was detected at the tumor, which could be clearly demarcated from the surrounding tissue. The *ex vivo* images of major organs and the tumor harvested at 24 h post-injection, the organ distribution of CRET-NPs. Interestingly, there was no significant difference in the *in vivo* biodistribution and *ex vivo* organ distribution between Ce6-NPs and CRET-NPs.

Table S1. Physicochemical characterization of CRET-NPs.

Sample	Diameter (nm)[a]	Zeta potential (mV)[b]	Degree of substitution (%)[c]	Weight %[c]
Ce6-NP	117.3 ± 8.84	-25.1 ± 0.71	7.2	10.2
CRET-NP	128.5 ± 7.48	-8.54 ± 0.53	-	-

[a] Measured by DLS
[b] Measured by zeta potential analyzer.
[c] Calculated by ^{1}H NMR.

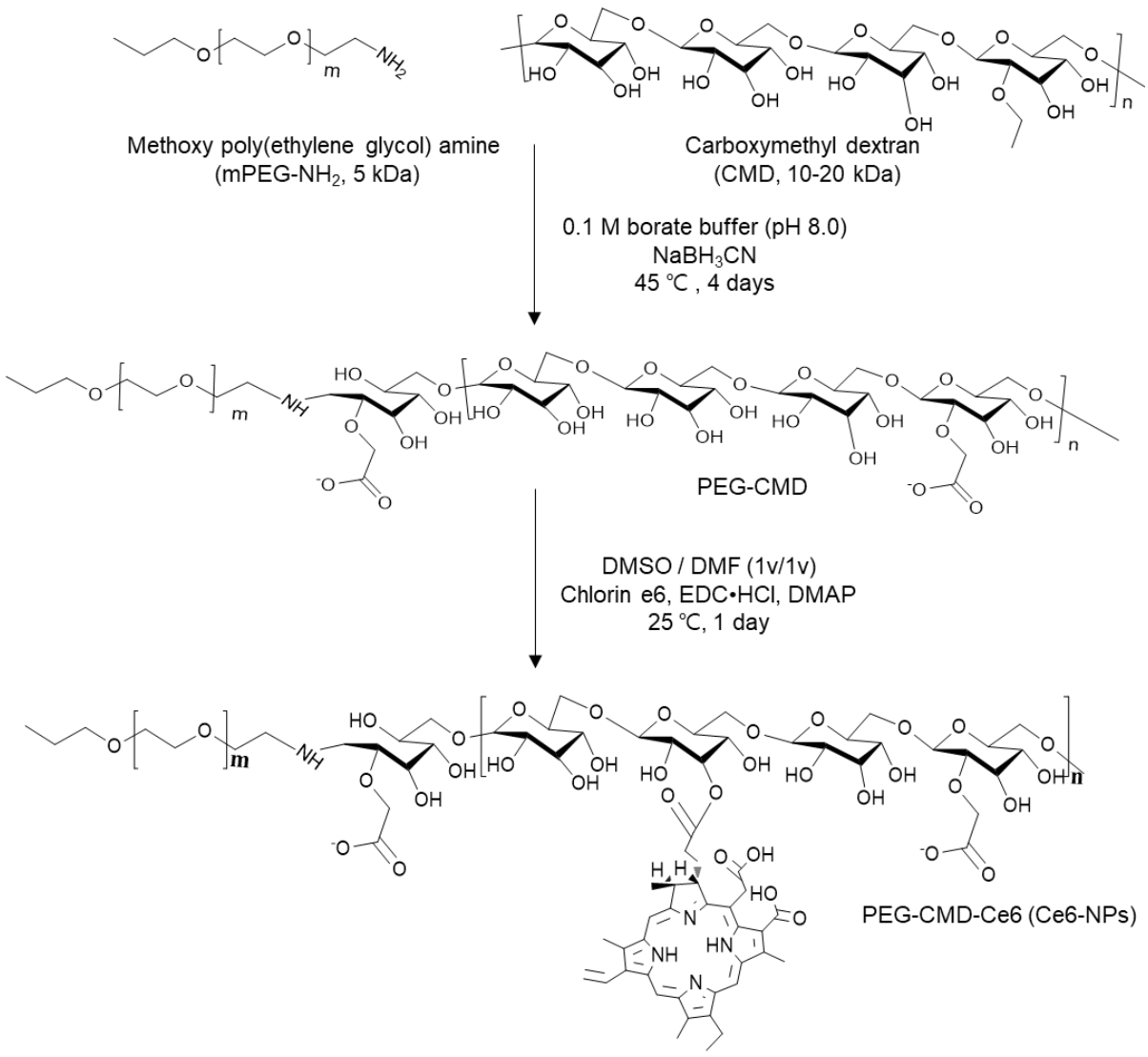

Fig. S1. Synthetic route of PEG-CMD-Ce6.

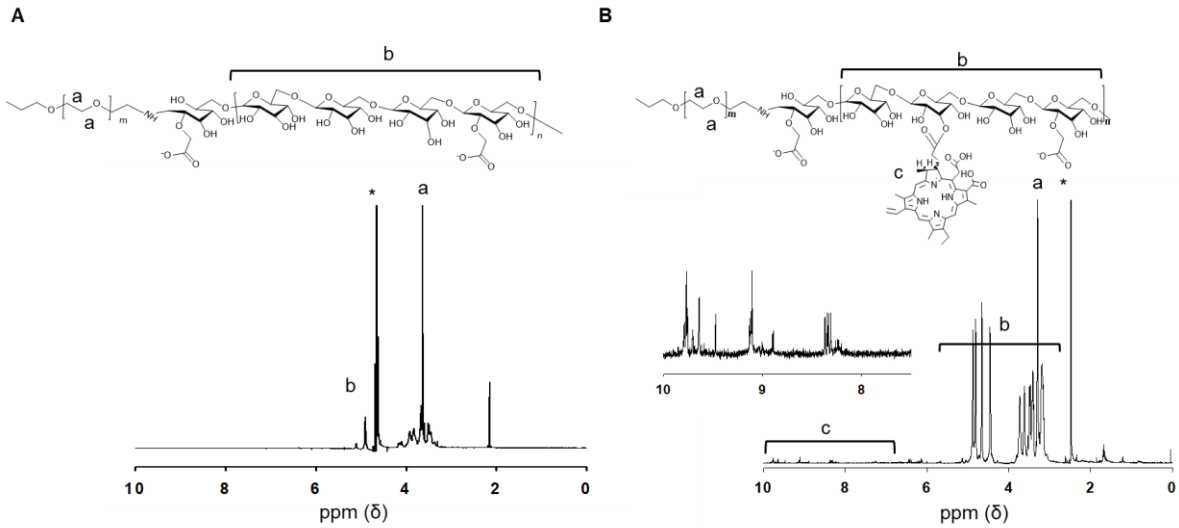

Fig. S2. ^{1}H NMR spectra of (A) PEG-CMD and (B) PEG-CMD-Ce6.

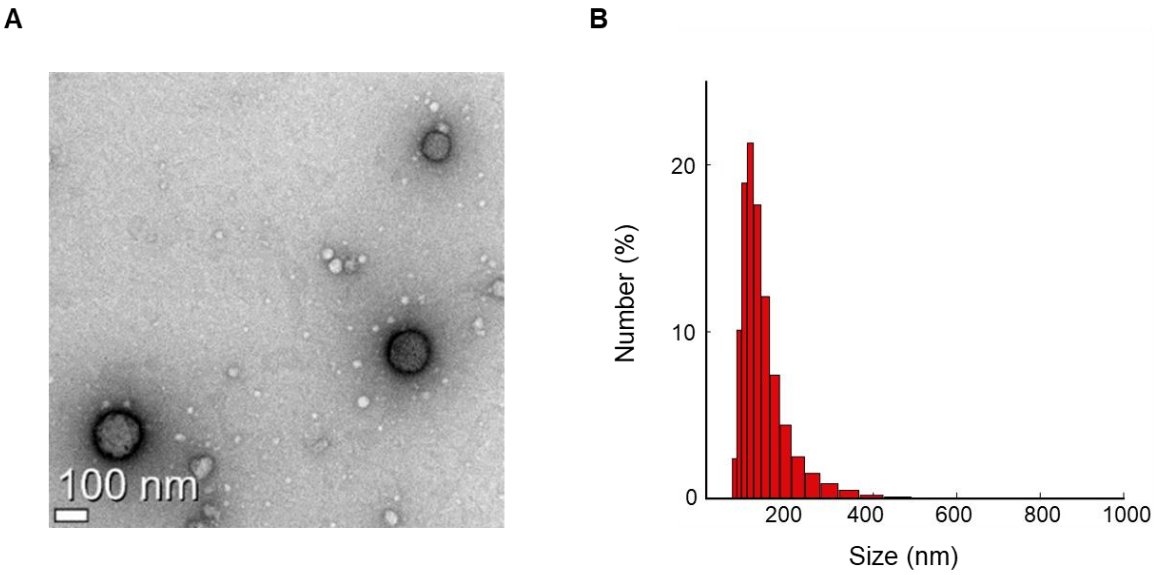

Fig. S3. Physicochemical characteristics of Ce6-NPs. (A) TEM image and (B) size distribution of Ce6-NPs.

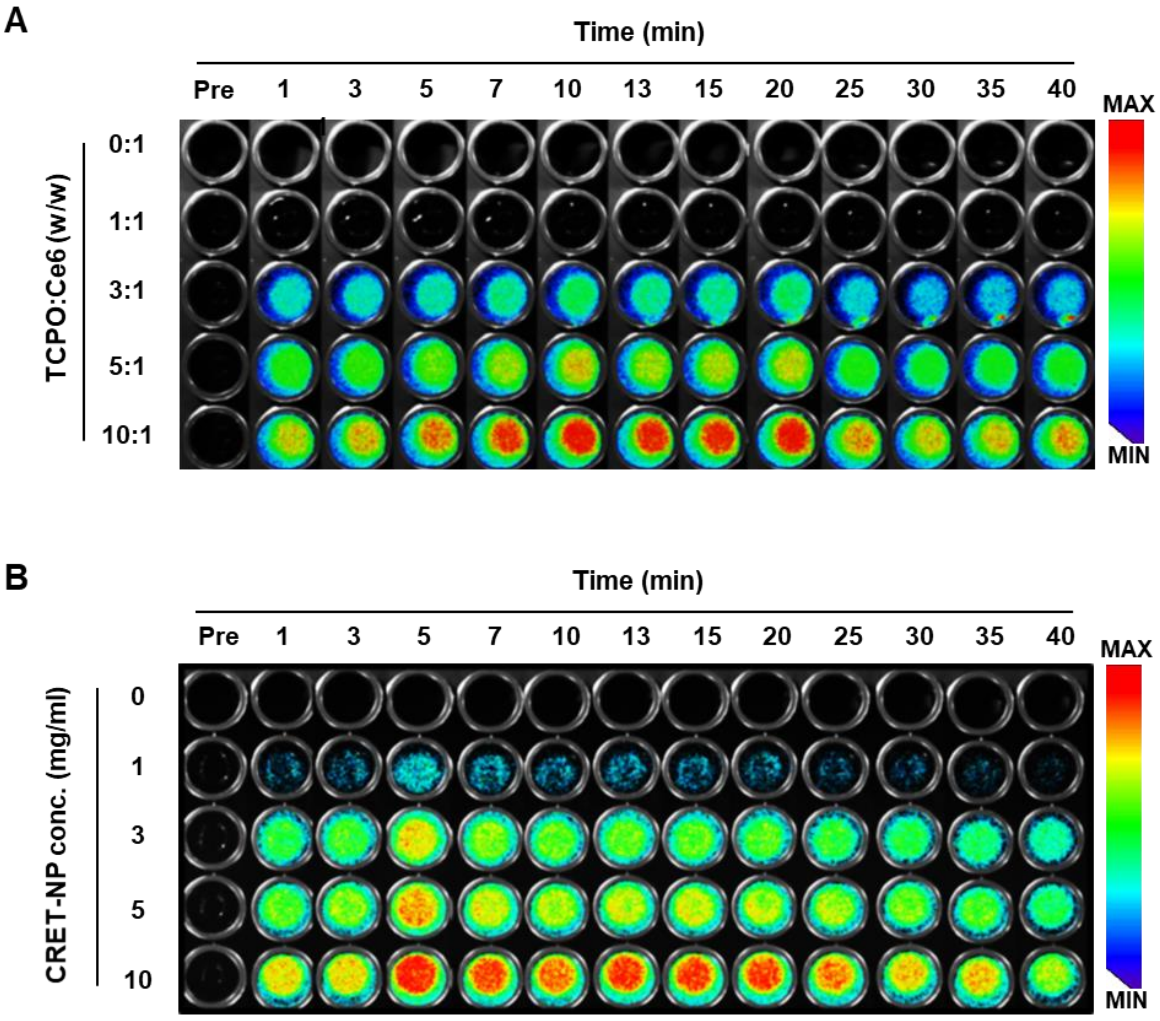

Fig. S4. *In vitro* CL imaging of CRET-NPs. (a) CL image at various ratios of TCPO in the presence of H_2O_2. (b) CL image at various concentrations of CRET-NPs.

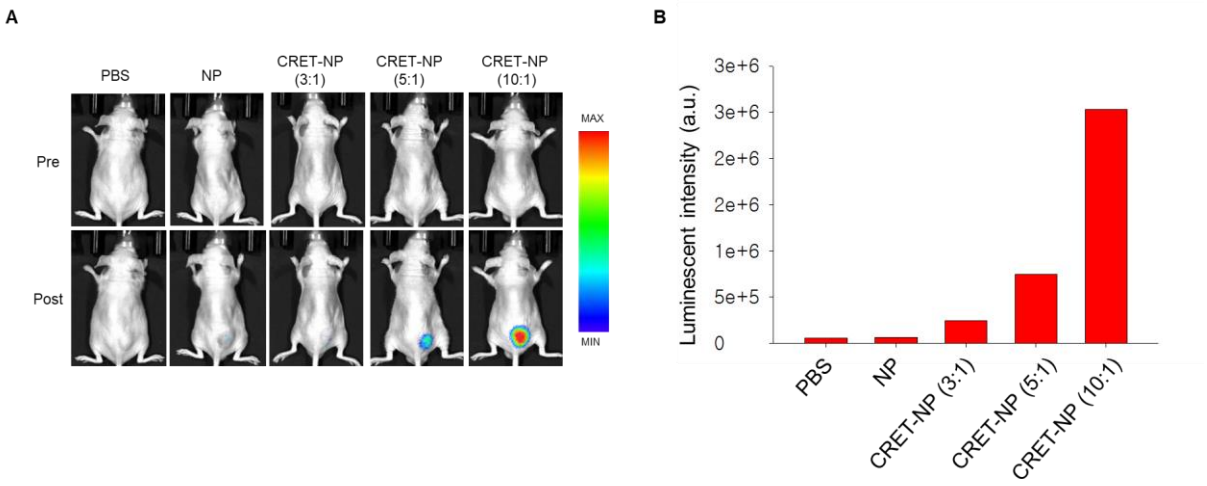

Fig. S5. *In vivo* CL imaging of CRET-NPs. (a) CL images after subcutaneous injection of CRET-NPs at various ratios of TCPO in the presence of H_2O_2. (b) Quantification of CL intensities of CRET-NPs at various ratios of TCPO.

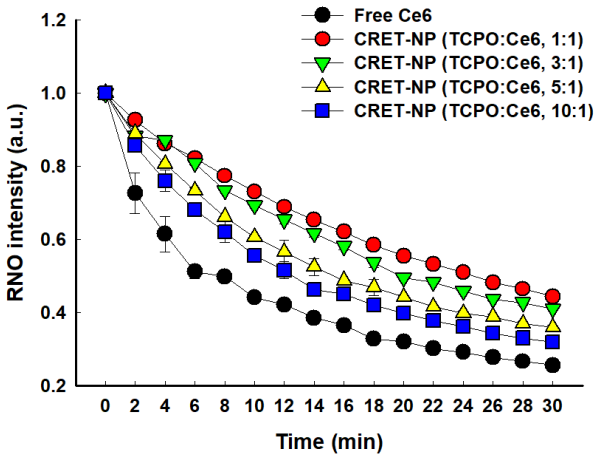

Fig. S6. ROS generation of CRET-NPs at various ratios of TCPO.

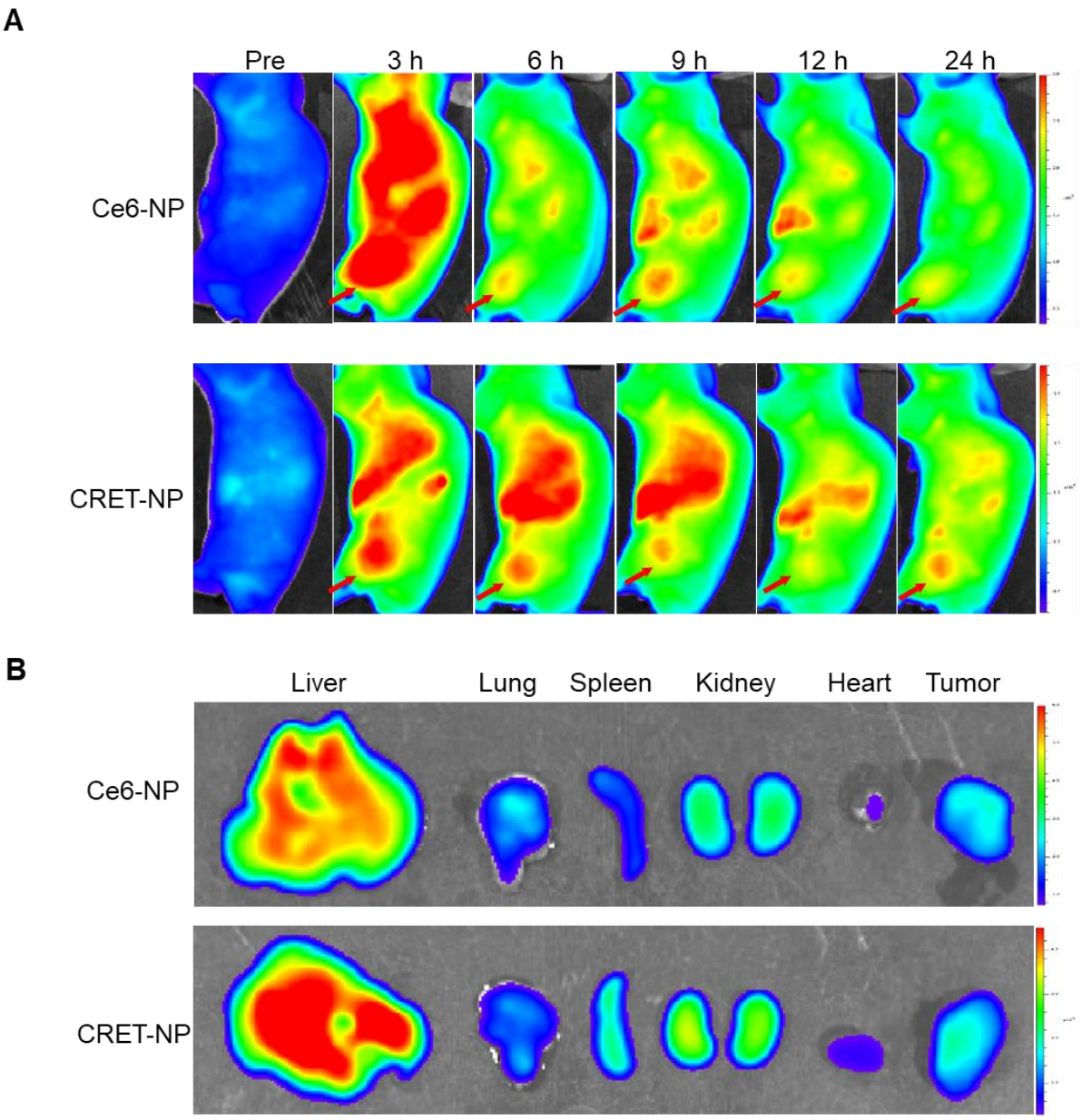

Fig. S7. Fluorescence imaging of CRET-NPs. (A) *In vivo* distribution of Ce6-NPs and CRET-NPs. (B) *Ex vivo* organ distribution of Ce6-NPs and CRET-NPs. The arrow indicates the tumoral region.

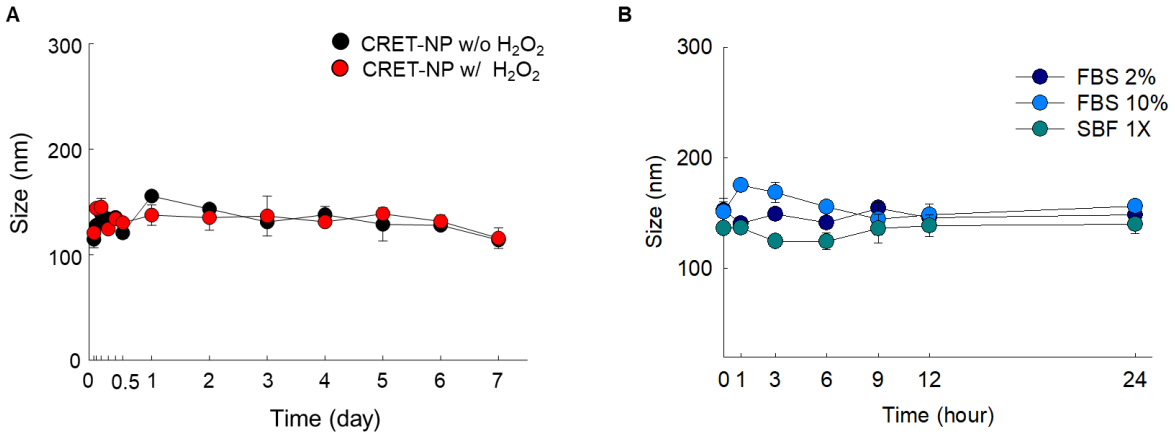

Fig. S8. Stability test of CRET-NPs. (A) Changes in particle size of CRET-NPs in PBS (pH 7.4). Error bars represent the standard deviation (n = 5). (B) Changes in particle size of CRET-NPs in standard simulated body fluid (SBF) and FBS-containing buffer. Error bars represent the standard deviation (n = 3).

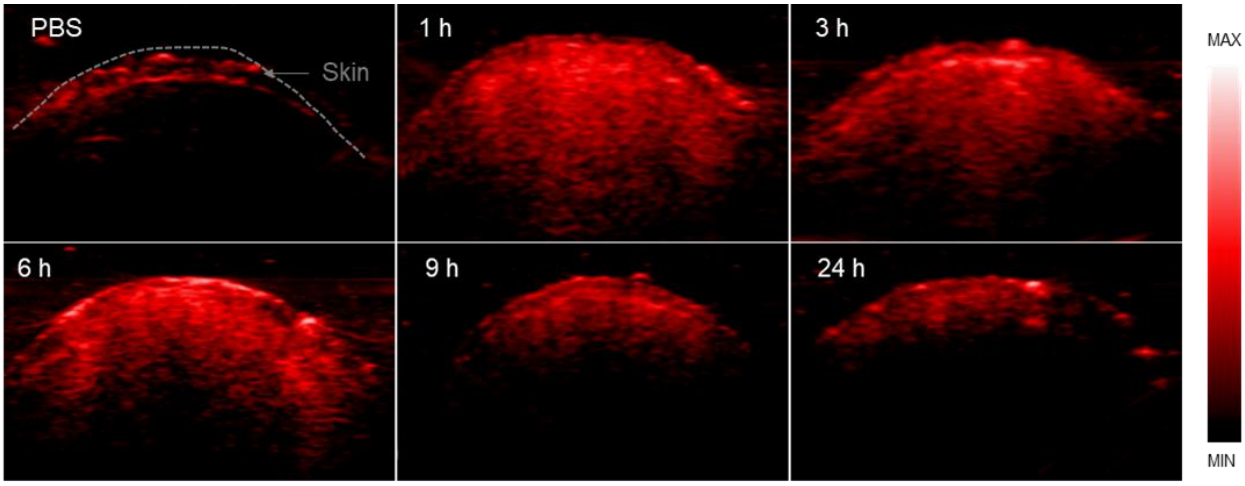

Fig. S9. *In vivo* PA images of CRET-NPs after their subcutaneous injection in the presence of H_2O_2.

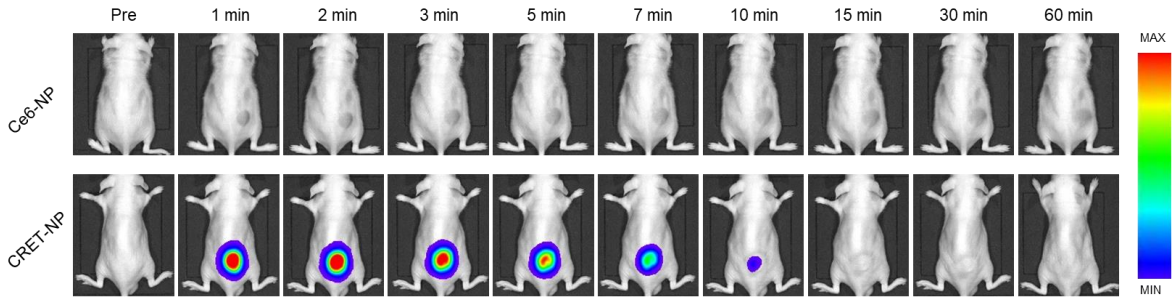

Fig. S10. *In vivo* CL images of CRET-NPs after their subcutaneous injection in the presence of H_2O_2.

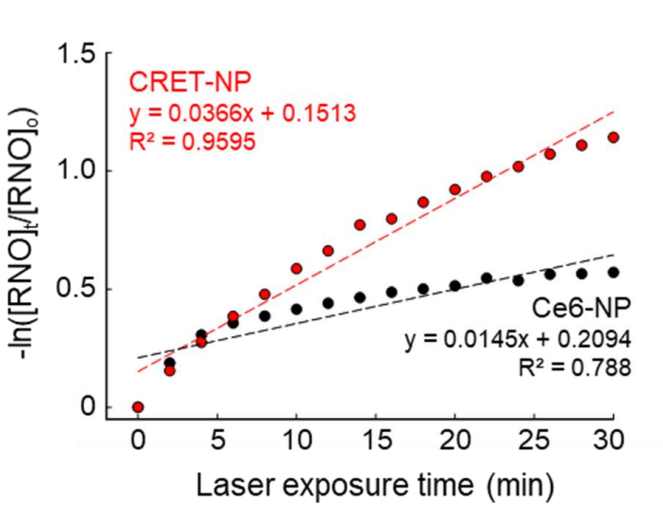

Fig. S11. First-order plot of RNO absorbance of Ce6-NPs and CRET-NPs as a function of time.

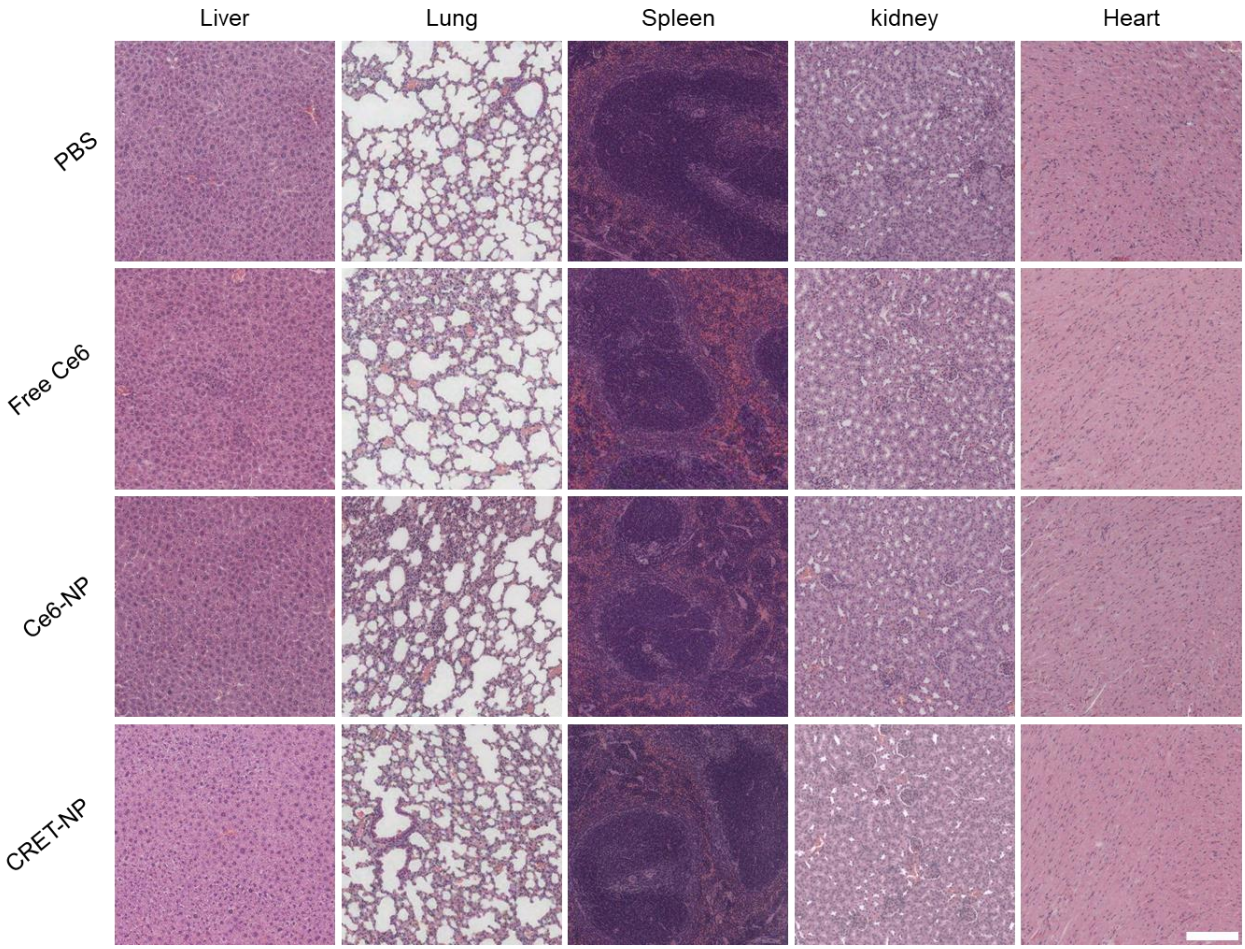

Fig. S12. H&E staining images of major organs after PDT with CRET-NPs in the absence of laser irradiation. The scale bar represents 200 μm.

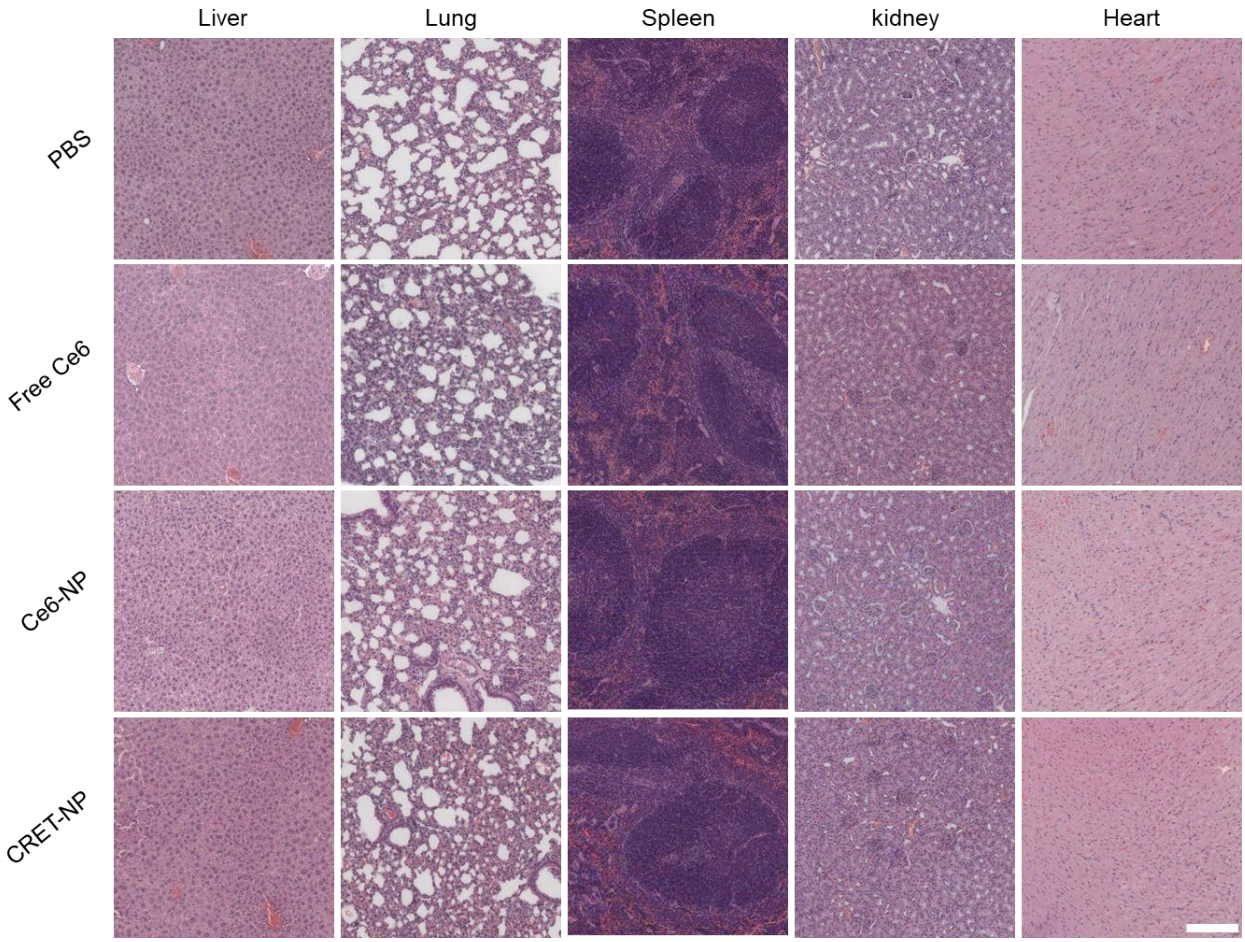

Fig. S13. H&E staining images of major organs after PDT with CRET-NPs under laser irradiation. The scale bar represents 200 μm.

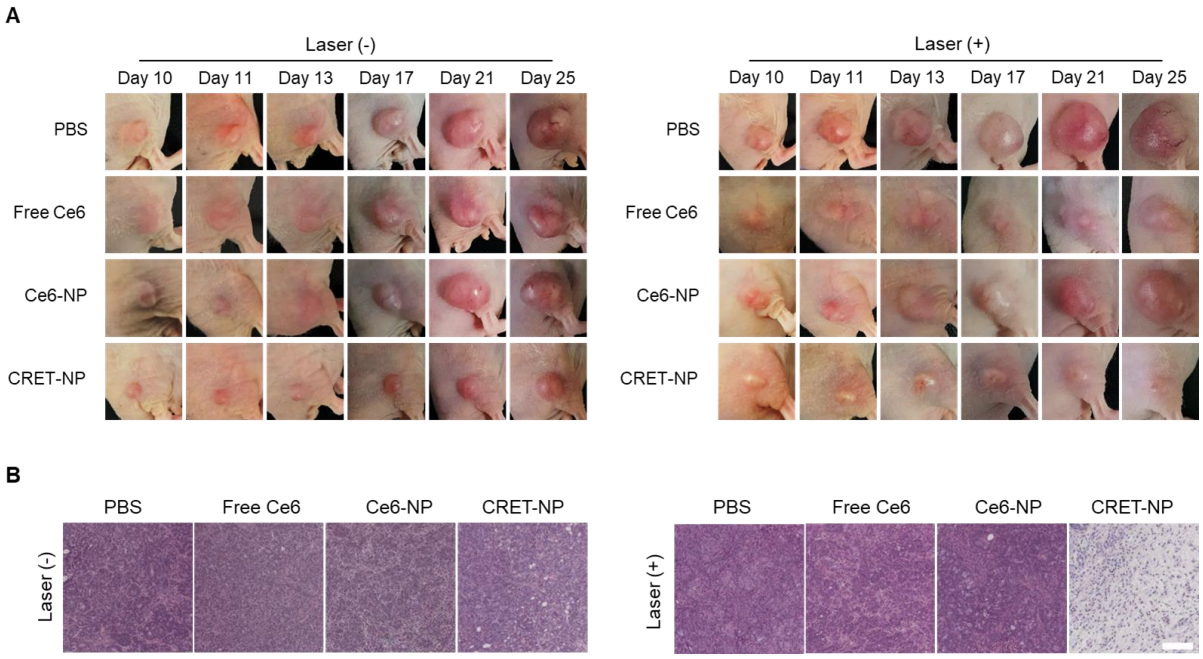

Fig. S14. Therapeutic efficacy of PDT with CRET-NPs. (A) Representative pictures of HT29 tumor-bearing mice during PDT. (B) H&E staining images of tumor tissues after PDT. The scale bar represents 200 μm. Photo credit: Jueun Jeon, Sungkyunkwan University